Wiley
International Journal of Energy Research
Volume 2025, Article ID 6685212, 15 pages
https://doi.org/10.1155/er/6685212

WILEY

Research Article

Impact of Phosphide–Phosphate Ratio on NiCoP Catalysts for Hydrogen Evolution in Anion Exchange Membrane Water Electrolysis

Taeyoung Kim,[1] **Kyeong-Rim Yeo**,[1] **Hoyoung Kim**,[2] **Jinwoo Lee**,[2] **and Soo-Kil Kim**[1]

[1]*School of Integrative Engineering, Chung-Ang University, Seoul 06974, Republic of Korea*
[2]*Department of Chemical and Biomolecular Engineering, Korea Advanced Institute of Science and Technology (KAIST), Daejeon 34141, Republic of Korea*

Correspondence should be addressed to Jinwoo Lee; jwlee1@kaist.ac.kr and Soo-Kil Kim; sookilkim@cau.ac.kr

Received 22 April 2025; Revised 11 June 2025; Accepted 19 June 2025

Academic Editor: Suresh Kannan Balasingam

Alkaline and anion exchange membrane water electrolysis (AEMWE) presents a promising approach for hydrogen production. However, the slow kinetics of the alkaline hydrogen evolution reaction (HER) remains a significant challenge. This study aimed to enhance HER activity by optimizing transition metal-phosphorus compound catalysts, including Ni, Co, NiCo, NiP, CoP, and NiCoP. Their surface structure, crystallinity, electrochemical properties, and HER performance were meticulously studied. Among the catalysts, $Ni_{28}Co_{62}P_{10}$ exhibited exceptional HER performance, achieving a low overpotential of 48 mV at a current density of $-10\,mA\,cm^{-2}$ in 1 M KOH. X-ray photoelectron spectroscopy analysis revealed that an optimal 1:1 balance of phosphate to phosphide is critical for achieving efficient HER. These findings emphasize the importance of balancing phosphorus species for optimal alkaline HER catalysis. Moreover, $Ni_{28}Co_{62}P_{10}$ demonstrated excellent durability, maintaining high performance after 5000 cycles. In AEMWE single-cell tests, the catalyst achieved a cell voltage of 1.88 V at $1\,A\,cm^{-2}$, surpassing the performance of Ni/Co-based catalysts from previous studies. The NiCoP-based catalysts in this study presented considerable promise for AEMWE systems, paving the way to the development of more efficient and durable catalysts for hydrogen production and advancing hydrogen-based renewable energy technologies.

Keywords: anion exchange membrane water electrolysis; electrocatalyst; electrodeposition; hydrogen evolution reaction; NiCoP

1. Introduction

Accelerated global warming due to CO_2 emissions from fossil fuel consumption has heightened the urgency for renewable energy development. While renewable energy sources do not generate greenhouse gases, their intermittent characteristic poses challenges for direct integration into the power grid, thereby necessitating stable energy storage systems (ESSs) [1, 2]. Compared to conventional secondary battery-based ESS, hydrogen offers significant advantages, including high energy density, long-term stable storage, and eco-friendliness [3, 4].

Traditionally, hydrogen production for industrial applications has relied on fossil fuel reforming. However, for ESS applications, renewable energy-driven water electrolysis is considered the most viable approach [5, 6]. Based on electrolyte type and operating temperature, water electrolysis can be classified into alkaline water electrolysis, anion exchange membrane water electrolysis (AEMWE), proton exchange membrane water electrolysis (PEMWE), and solid oxide electrolysis. Among these, AEMWE and PEMWE, which utilize polymer electrolyte membranes, have garnered significant research interest owing to their high current density, high-purity hydrogen production, and relatively low operating temperatures compared to other water electrolysis methods [7–10]. PEMWE is associated with high costs primarily due to the need for corrosion-resistant noble metal catalysts, which are

required to withstand the harsh acidic operating environment [11, 12]. In contrast, AEMWE offers a significant advantage by operating in a less corrosive alkaline environment, thus alleviating the dependence on expensive noble metals and reducing overall system costs [13, 14]. However, operating in a less corrosive environment does not inherently guarantee rapid electrode reaction kinetics. AEMWE involves a water dissociation step in the cathodic reaction, making the hydrogen evolution reaction (HER) significantly slower than in PEMWE [15].

Alkaline HER has been extensively studied and has been known to follow the Volmer step, wherein water dissociates to form an adsorbed hydrogen intermediate (H_{ads}), followed by either the Heyrovsky step or the Tafel step, leading to hydrogen evolution [16]:

$$\text{Volmer step}: H_2O + e^- \rightarrow H_{ads} + OH^-, \quad (1)$$

$$\text{Heyrovsky step}: H_2O + e^- + H_{ads} \rightarrow H_2 + OH^-, \quad (2)$$

$$\text{Tafel step}: H_{ads} + H_{ads} \rightarrow H_2. \quad (3)$$

Thus, achieving an optimal balance between water dissociation and hydrogen/hydroxyl adsorption is critical for efficient alkaline HER [17–19]. Research on alkaline HER catalysts has focused on developing transition metal alloys, transition metal compounds, and strategies to reduce noble metal content [20–23].

$MoNi_4@MoO_{3-X}$ exhibits an overpotential of 58.6 mV at –10 mA cm^{-2} in 1 M KOH, where the Ni component of the Ni-Mo alloy facilitates water dissociation, while the Mo phase plays a pivotal role in hydrogen adsorption, as highlighted in recent studies [22]. Furthermore, $Pt_{2.3\%}$-$Fe_{0.05}Ni_{0.95}(OH)_2$ catalyst effectively reduces the noble metal Pt content to 7.36 μg cm^{-2}. The synergistic interaction between Fe-doped α-$Ni(OH)_2$, which promotes water dissociation, and Pt nanoparticles, which facilitate H recombination, significantly enhances HER activity, achieving an overpotential of 18 mV at–10 mA cm^{-2} in 1 M KOH [23]. Extensive research has been conducted on transition metal compounds, particularly phosphides, sulfides, and carbides [24–29].

Transition metal phosphides (TMPs) exhibit promising catalytic properties, with Ni_2P-MoP@NC optimizing hydrogen adsorption energy (ΔG_{H^*}), thus achieving a favorable balance between adsorption and desorption. This optimization also reduces the water dissociation energy barrier, significantly accelerating the Volmer step. As a result, Ni_2P-MoP@NC demonstrates an overpotential of 69 mV at –10 mA cm^{-2} in 1 M KOH [28]. In addition, CoP-400, utilizing P doping, enhances hydrogen adsorption at P-top sites and water dissociation at Co-bridge sites, thereby improving catalytic performance under both acidic and alkaline conditions. This synergy enables CoP-400 to achieve low overpotentials of 113, 154, and 161 mV at −10 mA cm^{-2} in 0.5 M H_2SO_4, 1 M KOH, and 1 M phosphate buffer solution, respectively [27]. Moreover, the high electronegativity of phosphorus modified the electronic structure of the transition metal Ni, reducing the absolute values of the Gibbs free energy of hydrogen adsorption (ΔG_{H^*}), thereby achieving an overpotential of 59.7 mV at −10 mA cm^{-2} in 1 M KOH [29].

As aforedescribed, balancing water dissociation and hydrogen/hydroxyl adsorption is crucial for effective alkaline HER catalysis, making research on phosphides significant. Despite the importance of TMPs, limited studies have explored the impact of different phosphorus species, such as phosphide (P^{3-}), phosphite (PO_3^{3-}), and phosphate (PO_4^{3-}), on catalytic activity. Phosphate has been reported to act as a proton shuttle in alkaline HER, effectively weakening O–H bonds and stabilizing intermediates formed in the Volmer step, thereby lowering the activation barrier for water dissociation and accelerating the reaction [30–32]. Meanwhile, phosphides enhance the overall electronic conductivity by withdrawing electrons from transition metals because of their high electronegativity, optimizing hydrogen intermediate adsorption energy, and promoting the Tafel/Heyrovsky steps [33–35].

This study aimed to investigate the effect of various phosphorus species, particularly the ratio of phosphate to phosphide, on balancing the two key stages of alkaline HER. While previous studies on NiP and CoP have focused on the metal-to-phosphorus ratio [36–39], this study examined the electrochemical and material properties of bimetallic phosphorus-based compounds and their individual components. The findings were validated not only at the half-cell level but also in a full-cell configuration, affording deeper insights into phosphorus-based catalysts and aiding in maximizing their efficiency in alkaline HER.

2. Experimental

2.1. Catalyst Preparation. Ni, Co, NiCo, NiP, CoP, and NiCoP catalysts were synthesized via electrodeposition using a standard three-electrode setup at room temperature under atmospheric conditions. The catalysts were deposited onto carbon paper (Ballard, Avcarb MGL280) without surface pretreatment, serving as the working electrode with an active area of 1.327 cm^2. A graphite rod functioned as the counter electrode, while a saturated calomel electrode (SCE, CHI Instruments, CHI150) was used as the reference electrode.

The electrolyte solution was prepared by dissolving appropriate amounts of NH_4Cl (Daejung, 1060–4100), $NaH_2PO_2 \cdot H_2O$ (Yakuri Pure Chemicals Co. Ltd., 51519), $CoCl_2 \cdot 6H_2O$ (Daejung, 2570–4405), and $NiCl_2 \cdot 6H_2O$ (Wako Pure Chemical Industry, 141–01045) in deionized water (DI water, 18.2 MΩ), followed by stirring for 10 min. Detailed electrolyte compositions are provided in Table S1. Before electrodeposition, the electrolyte was purged with N_2 gas for 30 min to remove the dissolved O_2. Electrodeposition was performed using three potential cycles between −0.1 and −1.8 V_{SCE} at a scan rate of 5 mV s^{-1} using a potentiostat (Metrohm, Autolab, PGSTAT302N).

2.2. Material Characterization. The surface morphologies of the synthesized catalysts were analyzed using field emission scanning electron microscopy (FE-SEM; Carl Zeiss, Sigma 300), while their compositions were determined via energy-dispersive X-ray spectroscopy (EDS; Thermo, NORAN System 7). Crystallinity was assessed using X-ray diffraction

(XRD; Bruker-AXS, NEW D8-Advance) at a scan rate of 1.5° min^{-1} over a two-theta range of 5°–80°. The electronic structure of the catalyst surfaces was characterized via X-ray photoelectron spectroscopy (XPS, Thermo-Fisher Scientific, K-alpha+). The spectra were calibrated to the C–C peak in the C 1s region at 284.8 eV, and peak deconvolution was performed using XPSPEAK 41 software.

2.3. Electrochemical Characterization. All electrochemical analyses were conducted at room temperature under atmospheric conditions. The prepared catalysts served as the working electrode, with a graphite rod as the counter electrode and a mercury/mercurous oxide electrode (Hg/HgO, RE-61AP) as the reference electrode. Applied potentials were converted to the reversible hydrogen electrode potential (E_{RHE}) using the equation:

$$E_{RHE} = E_{exp} + E^0_{ref} + 0.0592V \times pH,$$

where E_{exp} is the experimental potential relative to the reference electrode, E^0_{ref} is 0.098 V for Hg/HgO, and pH is the electrolyte pH.

HER activity was evaluated using cyclic voltammetry over a single cycle, with a potential range of −0.85 to −1.25 $V_{Hg/HgO}$ at a scan rate of 1 mV s^{-1} under alkaline conditions (1 M KOH). Accelerated degradation tests (ADTs) for HER were conducted over 1000–5000 potential cycles at a scan rate of 100 mV s^{-1} over the same range. Additionally, constant current stability was assessed at −10 mA cm^{-2} for 24 h.

Electrochemical impedance spectroscopy was performed by applying a 30 mV DC overpotential with a 5 mV AC amplitude across a frequency range of 10^5–10^{-2} Hz in 1 M KOH using a potentiostat (Wuhan Corrtest Instruments Corp. Ltd, CS310). The obtained solution resistance (R_s) was used for iR correction. The double-layer capacitance (C_{dl}) was determined from linear sweep voltammetry (LSV) measurements, where the potential was first swept in the positive direction in the non-faradaic region and then reversed. The scan rate varied from 20 to 100 mV s^{-1}, and the electrochemically active surface area (ECSA) was evaluated by plotting half the difference between the anodic and cathodic currents ($[i_a - i_c]/2$) at the midpoint of the potential range as a function of the scan rate.

2.4. AEMWE Operation. A membrane electrode assembly (MEA) was fabricated without hot pressing, incorporating a 1×1 cm^2 cathode and anode on either side of a 20 μm-thick PiperION anion exchange membrane. The cathode utilized the $Ni_{28}Co_{62}P_{10}$/CP electrode, the highest-performing catalyst developed in this study.

For anode fabrication, catalyst ink was prepared by dispersing Ni_2Fe_1 powder [40] and PiperION dispersion (5 wt%) in a solvent mixture of DI water, ethanol, and isopropyl alcohol at a 1:1:2 volume ratio. This was designed to achieve a solid content of 2 wt% with a Ni_2Fe_1 to ionomer mass ratio of 9:1. The resultant suspension was sonicated for 1 h to ensure homogeneous distribution. The ink was applied via handgun spraying onto a 600 μm-thick stainless steel (SS) fiber felt (Dioxide Materials), yielding a Ni_2Fe_1/SS anode with a catalyst loading of 3.0 mg cm^{-2}.

To convert the ionically conductive components from the bicarbonate to the hydroxide (OH^-) form, the anode and membrane were immersed in a 1.0 M KOH solution at room temperature for 12 h under sealed conditions, followed by thorough rinsing with DI water.

The AEMWE cell was assembled with a clamping torque of 80 IN•LB, utilizing 215 μm-thick and 600 μm-thick polytetrafluoroethylene (PTFE) gaskets for the cathode and anode, respectively. A preheated 1.0 M KOH solution was supplied to the anode side at a flow rate of 3 mL min^{-1}, maintaining the cell temperature at 80°C. The current–voltage (*I–V*) curve was recorded by averaging the current density over 1 min at each voltage step, at 50 mV increments within a voltage range of 1.35–2.1 V_{cell}. For durability assessment, the cell operated at a constant current density of 1.0 A cm^{-2} for 100 h.

3. Results and Discussion

The FE-SEM images in Figure 1 show the surface morphology of representative samples, along with their atomic compositions determined via EDS analysis. For Ni_{100}, owing to its relatively positive reduction potential (−0.257 V vs. SHE), a significant amount of Ni ions is reduced during electrodeposition at –1.8 V_{SCE}. The fibrous structure of the underlying carbon paper is then completely obscured, forming a thick electrodeposited layer with a cracked film structure. Porous aggregates are also observed on the noncracked regions of the deposited layer. In contrast, Co_{100}, which has a more negative reduction potential and a lower precursor concentration compared to Ni_{100}, forms agglomerated particles rather than the bulky deposition observed in Ni_{100}. This allows for partial visibility of the carbon fibers beneath the deposited layer. The particulate deposition of Co is attributed to the use of $CoCl_2$ as the Co precursor [41]. The morphology significantly transforms upon incorporating a small amount of P, as observed in the case of $Ni_{92}P_8$. A similar morphological change is observed in $Co_{97}P_3$, attributed to the inhibition of Ni_{ad} [42] and Co_{ad} [43] diffusion by the introduced P. This leads to a more controlled deposition process, resulting in either fiber-aligned deposition along the carbon paper (NiP) or the formation of smaller agglomerated deposits (CoP). For $Ni_{66}Co_{34}$, anomalous deposition occurs, where the less noble metal (Co) is preferentially deposited. This phenomenon is attributed to pH variations near the electrode surface and the competitive adsorption of metal hydroxyl species [44, 45]. As a result, the bulk molar concentration ratio of the deposited catalyst (Ni:Co = 66:34) deviates considerably from the nominal electrolyte composition (Ni:Co = 0.5:0.15). Consequently, the preferential deposition of Co suppresses the overdeposition of Ni, preventing excessive deposition as observed in Ni_{100}. This allows the deposition to follow the fibrous structure of the carbon paper. In $Ni_{28}Co_{62}P_{10}$, the smooth morphology of NiP and the particulate morphology of CoP interact, resulting in the coexistence of both structural features (uniform particulate deposition on the carbon fibers). Despite using the same concentration of metal ions, the Ni-to-Co ratio in $Ni_{28}Co_{62}P_{10}$

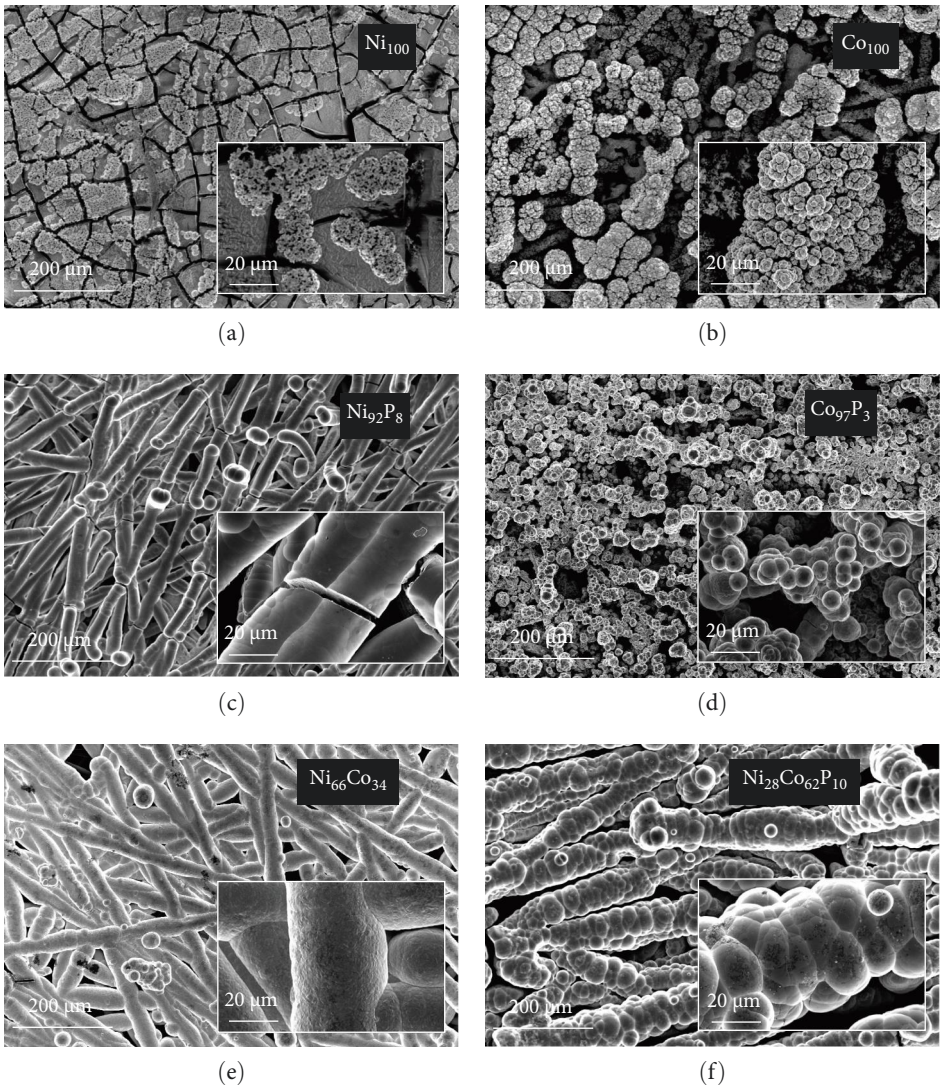

FIGURE 1: FE-SEM images of (a) Ni_{100}, (b) Co_{100}, (c) $Ni_{92}P_8$, (d) $Co_{97}P_3$, (e) $Ni_{66}Co_{34}$, and (f) $Ni_{28}Co_{62}P_{10}$. Insets show higher-magnification images.

is reversed compared to $Ni_{66}Co_{34}$. This reversal is attributed to the presence of P, which enhances the anomalous deposition, further promoting the preferential deposition of the less noble metal, Co [46]. Consequently, the deposited layer predominantly exhibits a granular surface morphology characteristic of Co. EDS elemental mapping (Figure S1) further confirms that Ni, Co, and P are uniformly distributed across the surface without signs of phase separation. This supports the formation of a homogeneous NiCoP structure.

Figure 2 presents the XRD analysis results used to investigate the crystallinity of each catalyst. For the carbon paper, typical peaks are observed at 43.02°, 44.67°, and 54.79°. In the case of Ni_{100}, the peaks at 44.51°, 51.85°, and 76.4° correspond to Ni (111), (200), and (220) (JCPDS #04−0850), respectively. For Co_{100}, the peaks at 41.58°, 44.50°, and 47.44° correspond to Co (100), (002), and (101) (JCPDS 01-071-4239). However, the crystallinity of Co appears to be low. In $Ni_{66}Co_{34}$, due to the low Co content, only Ni peaks are observed at 44.41°, 51.79°, and 76.33°. Notably, the Ni (111) peak at 44.51° shifts by approximately 0.1° because of the alloying with Co. When phosphorus is introduced to the monometallic samples during deposition, the resulting XRD patterns differ significantly from those of the individual metals. In $Ni_{92}P_8$, a very broad peak is observed at 45.31°. The carbon peak at 44.67° is not visible, suggesting that this broad peak corresponds to that of Ni (111). The peak broadening suggests the underdevelopment of the crystalline structure due to the incorporation of phosphorus [42], as observed in the FE-SEM images in Figure 1. The grain sizes, calculated from the full width at half maximum of the Ni (111) peak, are 14.9 nm for Ni and 1.8 nm for $Ni_{92}P_8$. In contrast to Co_{100}, which showed some crystallinity, $Co_{97}P_3$ exhibits a structure that is closer to amorphous, as does $Ni_{28}Co_{62}P_{10}$. The excellent HER activity of amorphous catalysts has been widely documented in numerous studies [47, 48]. For most of the samples, the underlying carbon peak is not observed because of the thick deposition layer.

Figure 3a displays the iR-corrected HER polarization curves of several representative catalysts. The HER activity

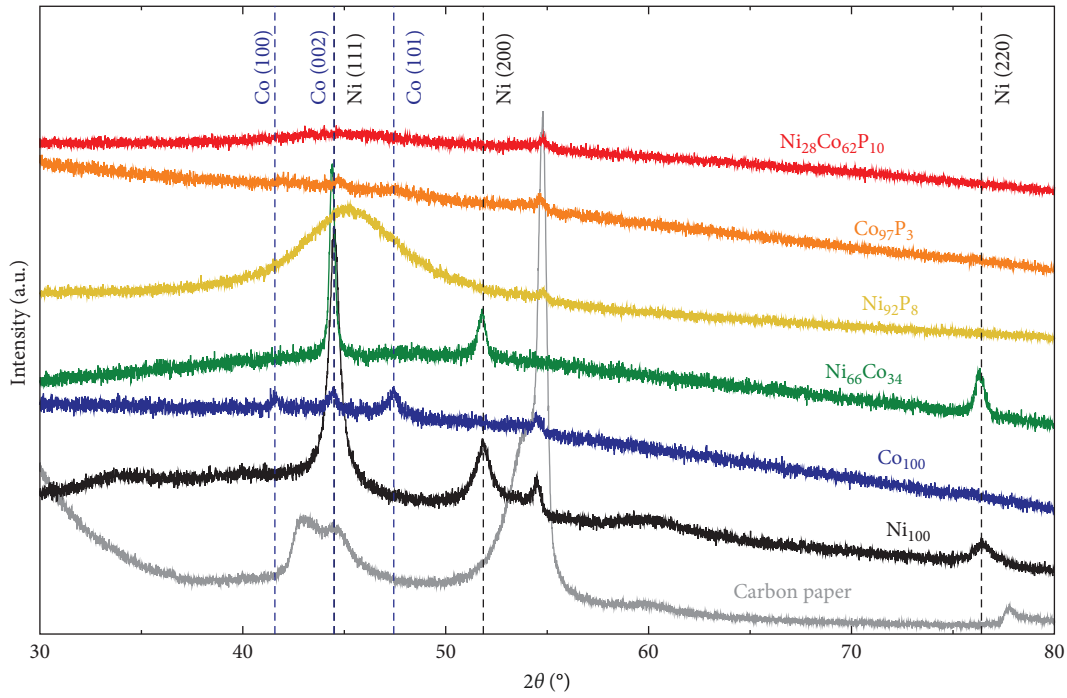

FIGURE 2: XRD patterns of carbon paper, Ni_{100}, Co_{100}, $Ni_{66}Co_{34}$, $Ni_{92}P_8$, $Co_{97}P_3$, and $Ni_{28}Co_{62}P_{10}$.

evaluations were carried out in an alkaline environment (1 M KOH). The catalysts evaluated include Ni_{100}, Co_{100}, $Ni_{66}Co_{34}$, $Ni_{92}P_8$, $Co_{97}P_3$, and $Ni_{28}Co_{62}P_{10}$ (HER activity data for all synthesized catalysts are summarized in Table S1). The monometallic catalysts, Co_{100} and Ni_{100}, exhibited overpotentials of approximately 310 mV and 226 mV at $-10\ mA\ cm^{-2}$, respectively, indicating very low HER activity. The $Ni_{66}Co_{34}$ alloy showed a slightly improved overpotential of 294 mV at $-10\ mA\ cm^{-2}$ compared to Co_{100}. However, its activity remained inferior to that of Ni_{100} owing to the high Co content. This suggests that simple NiCo binary alloys are not optimal for effective alkaline HER catalysis. In contrast, the monometallic phosphorus compounds, $Ni_{92}P_8$ and $Co_{97}P_3$, exhibited significantly enhanced activity, with overpotentials of 84 mV and 87 mV at $-10\ mA\ cm^{-2}$, respectively. These values represent improvements of 142 and 223 mV compared to their respective monometallic counterparts, confirming that even a small incorporation of phosphorus can substantially boost alkaline HER performance. This enhancement has been widely observed in previous studies. For instance, a heat-treatment phosphorization method was used to synthesize Ni_2P catalysts, which exhibited a 32 mV improvement in overpotential at $-10\ mA\ cm^{-2}$ compared to pure Ni [49]. Similarly, CoP_2 catalysts synthesized via heat-treatment phosphorization showed a remarkable 238 mV enhancement in HER activity compared to monometallic Co under alkaline conditions [50]. A noteworthy finding of our study is that the NiCo alloy, which exhibited lower activity than monometallic Ni because of its high Co content, demonstrated exceptional performance upon phosphorus incorporation. Specifically, $Ni_{28}Co_{62}P_{10}$ exhibited an overpotential of just 48 mV at $-10\ mA\ cm^{-2}$, surpassing the activity of both NiP and CoP. Thus, the formation mechanism of P-induced compounds in NiCo alloys differs fundamentally from that in monometallic Ni-based compounds, leading to superior catalytic performance.

Figure 3b presents the Tafel slope values for each catalyst, derived from the polarization curves in Figure 3a. The Tafel slopes for Ni_{100}, Co_{100}, and $Ni_{66}Co_{34}$ are 108, 200, and 188 mV dec^{-1}, respectively, indicating that the Volmer reaction is the rate-determining step. For $Ni_{92}P_8$, the Tafel slope is 68 mV dec^{-1}, which is lower than that of Ni_{100}, suggesting that the addition of a small amount of phosphorus shifts the HER mechanism from Volmer-limiting to Heyrovsky-limiting. In contrast, $Co_{97}P_3$ and $Ni_{28}Co_{62}P_{10}$ exhibit Tafel slopes of 32 mV dec^{-1}, indicating that the Tafel reaction is the rate-determining step [51]. Based on the HER polarization curves and Tafel slope values, the addition of phosphorus to a less active transition metal significantly accelerates the HER rate by altering the mechanism of water dissociation. This trend is further validated through comparative analysis with literature-reported NiCo-based phosphide/phosphate catalysts, as summarized in Table S2 and visualized in Figure S2. Furthermore, as previously discussed, the distinct compound formation between NiP and NiCoP plays a crucial role in influencing the HER reaction mechanism.

ECSA measurements were performed to explore the factors contributing to the varying HER activities of the catalysts. Figure 3c displays the C_{dl} values for each catalyst, derived from LSV conducted in the non-faradaic potential region of a 1 M KOH electrolyte (Figure S3). Ni_{100} and Co_{100} exhibit low C_{dl} values of 9.03 and 12 mF cm^{-2}, respectively. In contrast, the $Ni_{66}Co_{34}$ alloy shows a higher C_{dl} of 18.7 mF cm^{-2} compared to the monometallic catalysts. These trends are consistent with the catalyst surface morphologies observed in the SEM images in Figure 1. Specifically, Ni_{100}, with its plate-like deposition (Figure 1a), mitigates the area effect of the porous carbon

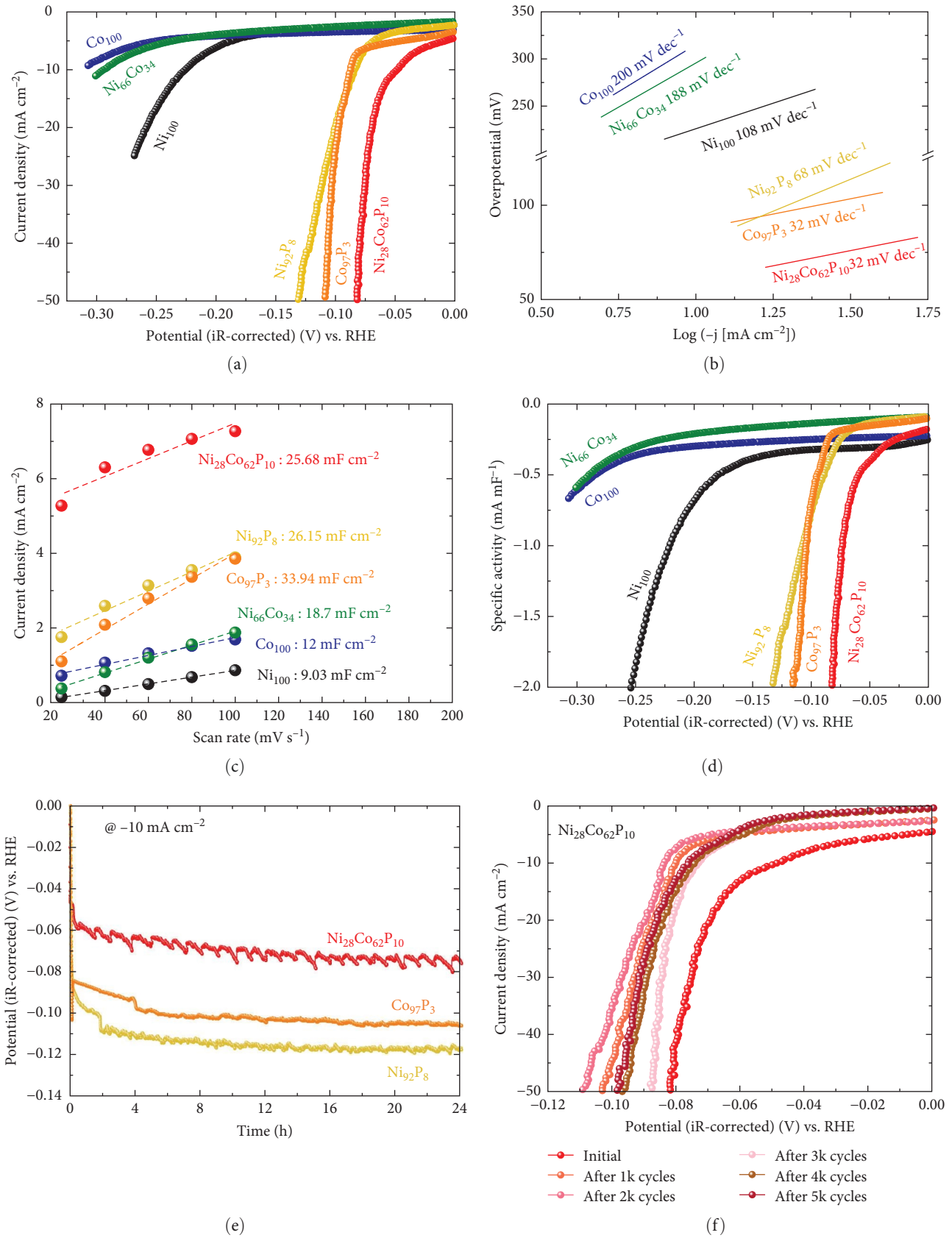

FIGURE 3: (a) HER polarization curves obtained by cyclic voltammetry at scan rate of 1 mV s^{-1} in 1 M KOH for Co_{100}, Ni_{100}, $Ni_{92}P_8$, $Co_{97}P_3$, $Ni_{66}Co_{34}$, and $Ni_{28}Co_{62}P_{10}$. (b) Corresponding Tafel plots. (c) Half current difference ($[i_a - i_c]/2$) versus scan rate for Co_{100}, Ni_{100}, $Ni_{92}P_8$, $Co_{97}P_3$, $Ni_{66}Co_{34}$, and $Ni_{28}Co_{62}P_{10}$. (d) Specific activity derived from the HER polarization curves of the corresponding catalysts. (e) Durability test by −10 mA cm^{-2} for 24 h in 1 M KOH ($Ni_{92}P_8$, $Co_{97}P_3$, $Ni_{28}Co_{62}P_{10}$). (f) Durability test by 1000–5000 potential cycling between −1.25 to −0.85 $V_{Hg/HgO}$ at a scan rate of 100 mV s^{-1} in the same electrolyte ($Ni_{28}Co_{62}P_{10}$).

paper. Meanwhile, Co_{100} (Figure 1b) shows a slight increase in surface area relative to Ni_{100} owing to its particulate morphology. Nevertheless, the bulky nature of its deposition prevents it from fully exploiting the structural advantages of the carbon fibers. In contrast, $Ni_{66}Co_{34}$, with limited deposition, maintains the carbon fiber structure, thus presenting a higher surface area.

For $Ni_{92}P_8$ and $Co_{97}P_3$, which incorporate phosphorus into the monometallic catalysts, there is a significant increase in C_{dl}. This is attributed to the well-developed pore structure of $Ni_{92}P_8$, which is deposited thinly along the carbon paper fibers (Figure 1c), and the high porosity of $Co_{97}P_3$, which forms smaller particle clusters (Figure 1d). Similarly, $Ni_{28}Co_{62}P_{10}$ exhibits a considerable C_{dl} of 25.68 mF cm^{-2}, and although its deposition is relatively thicker than that of $Ni_{92}P_8$ (Figure 1c) and $Co_{97}P_3$ (Figure 1d), resulting in a slightly lower C_{dl} than these catalysts, it still maintains a sufficiently high capacitance. Using the C_{dl} values from Figure 3c, the HER activity from Figure 3a was normalized to determine the specific activity, as shown in Figure 3d. While the specific activity of each catalyst follows a trend similar to that in Figure 3a. This statement suggests that metallic catalysts containing phosphorus not only have a relatively high ECSA but also possess other unique characteristics that enhance HER activity.

Figure 3e shows the results of the constant current durability test conducted for 24 h at −10 mA cm^{-2} on $Ni_{92}P_8$, $Co_{97}P_3$, and the most efficient HER catalyst, $Ni_{28}Co_{62}P_{10}$. During the 24 h constant current durability evaluation, both $Ni_{92}P_8$ and $Co_{97}P_3$ demonstrated a sudden potential decay at an early stage of test (around 2–4 h), indicating poor constant current durability. In contrast, $Ni_{28}Co_{62}P_{10}$ showed a stable potential with a decay rate of approximately 1.17 mV h^{-1}, suggesting superior durability compared to the monometallic NiP and CoP. This performance is more favorable than previously reported decay rates for metal phosphides, such as approximately 2.88 mV h^{-1} for Rh_2P [52] and 1.46 mV h^{-1} for O-NiCoP/Ni_2P [53].

In addition to the constant current durability test, an ADT was conducted for $Ni_{28}Co_{62}P_{10}$ within the potential range of −0.85 to −1.25 $V_{Hg/HgO}$ at a scan rate of 100 mV s^{-1}, as shown in Figure 3f. The $Ni_{28}Co_{62}P_{10}$ catalyst performance declined up to 2000 cycles, followed by a slight recovery, ultimately stabilizing. After 5000 cycles, the catalyst showed a 28 mV increase in overpotential at −10 mA cm^{-2}, with a decay rate of 5.6 μV per cycle.

XPS analysis was performed to investigate the factors contributing to the excellent HER activity and durability of the $Ni_{28}Co_{62}P_{10}$ catalyst. Figure 4 shows the XPS results of $Co_{97}P_3$, $Ni_{92}P_8$, and the most efficient HER catalyst, $Ni_{28}Co_{62}P_{10}$, before and after 5000 cycles of ADT evaluation. Additional XPS data for various compositions of NiCoP catalysts, prepared with different precursor configurations in the electrolyte, are provided in Figure S4, and their HER activities are shown in Figure S5. The overpotentials at −10 mA cm^{-2} for these catalysts are summarized in Table S1. A key focus of the XPS analysis in Figure 4 and Figure S4 is the relative ratio of phosphate and phosphide species. In our previous study on NiP [54], the formation of phosphate and phosphide was found to be potential-dependent, with more negative step potentials favoring phosphate formation and more positive potentials promoting phosphide. In the present work, the coexistence of both species was achieved by applying potential cycles between −0.1 and −1.8 V_{SCE} during electrodeposition. This behavior is attributed to local pH gradients generated by the HER, which create spatially distinct microenvironments across the electrode surface, favoring phosphide formation in more acidic regions and phosphate formation in more alkaline ones [55, 56]. Through XPS analyses of the various catalysts, we aim to correlate the presence ratios of phosphate and phosphide in each catalyst with their respective activity. The P 2p binding energy for $Ni_3(PO_4)_2$ or $Co_3(PO_4)_2$ is typically between 133–135 eV [57, 58], while for metal phosphides such as Ni_2P, Ni_5P_4, Co_2P, and CoP, the P 2p binding energy falls between 128–130 eV [59, 60]. Through these differences in characteristics, Figure 5 presents the relationships between the overpotential at −10 mA cm^{-2} and the phosphate peak area (Figure 5a), phosphide peak area (Figure 5b), and the phosphide/phosphate ratio (Figure 5c) based on the information obtained from Figure 4 and Figure S4. Several important conclusions can be drawn from Figure 5. First, HER activity shows no clear correlation with the EDS composition ratios of Ni, Co, and P in the catalysts. Second, HER activity tends to be proportional to the amount of phosphate, although there are several exceptions (Figure 5a). Third, HER activity exhibits a more clearly defined relationship with the amount of phosphide compared to phosphate, although there are some outlier samples ($Ni_{55}Co_{33}P_{12}$, $Ni_{19}Co_{73}P_8$) (Figure 5b). Lastly, HER activity shows a clear relationship with the phosphide/phosphate ratio, with only one exception ($Ni_{19}Co_{73}P_8$) (Figure 5c). These findings suggest that the activity of metal-phosphorus compound catalysts is more strongly influenced by the constituent species (phosphate and phosphide) rather than the metal itself. Metal phosphides are recognized as active sites for HER catalysis, playing a positive role by enhancing the electrical conductivity and promoting electrode reactions [17, 26, 61]. Metals with low oxidation states are known to form phosphides [62]; however, further oxidation of phosphides (e.g., due to the presence of oxygen or moisture) can lead to the formation of phosphates [63]. Metal phosphates are stable compounds with relatively lower hydrogen evolution activity than phosphides because of their lower conductivity [64, 65]. However, recent studies have highlighted the potential of transition metal phosphates as HER catalysts. Along with the previously mentioned advantages of phosphate as an alkaline HER catalyst [30–32], Wijayanti et al. demonstrated that the (100) and (011) facets of nickel phosphate are the most stable surface facets, and the weaker hydrogen adsorption energies at the oxygen sites on these facets enhance product desorption, thereby improving HER performance [66]. Furthermore, Xing et al. reported that the amorphous Ni-Fe phosphate film/Ni foam enhances ionic conductivity, stabilizes catalyst performance by uniformly depositing on the Ni foam, and acts as a protective layer, increasing durability and achieving excellent performance with an 87 mV overpotential at −10 mA cm^{-2} in 1 M KOH [67]. Additionally, Yang et al. [68] showed that the amorphous $FePO_4$ with a low d-band center energy level and low Gibbs free energy exhibits excellent electrocatalytic activity. These studies indicate that both TMPs and phosphates can contribute to

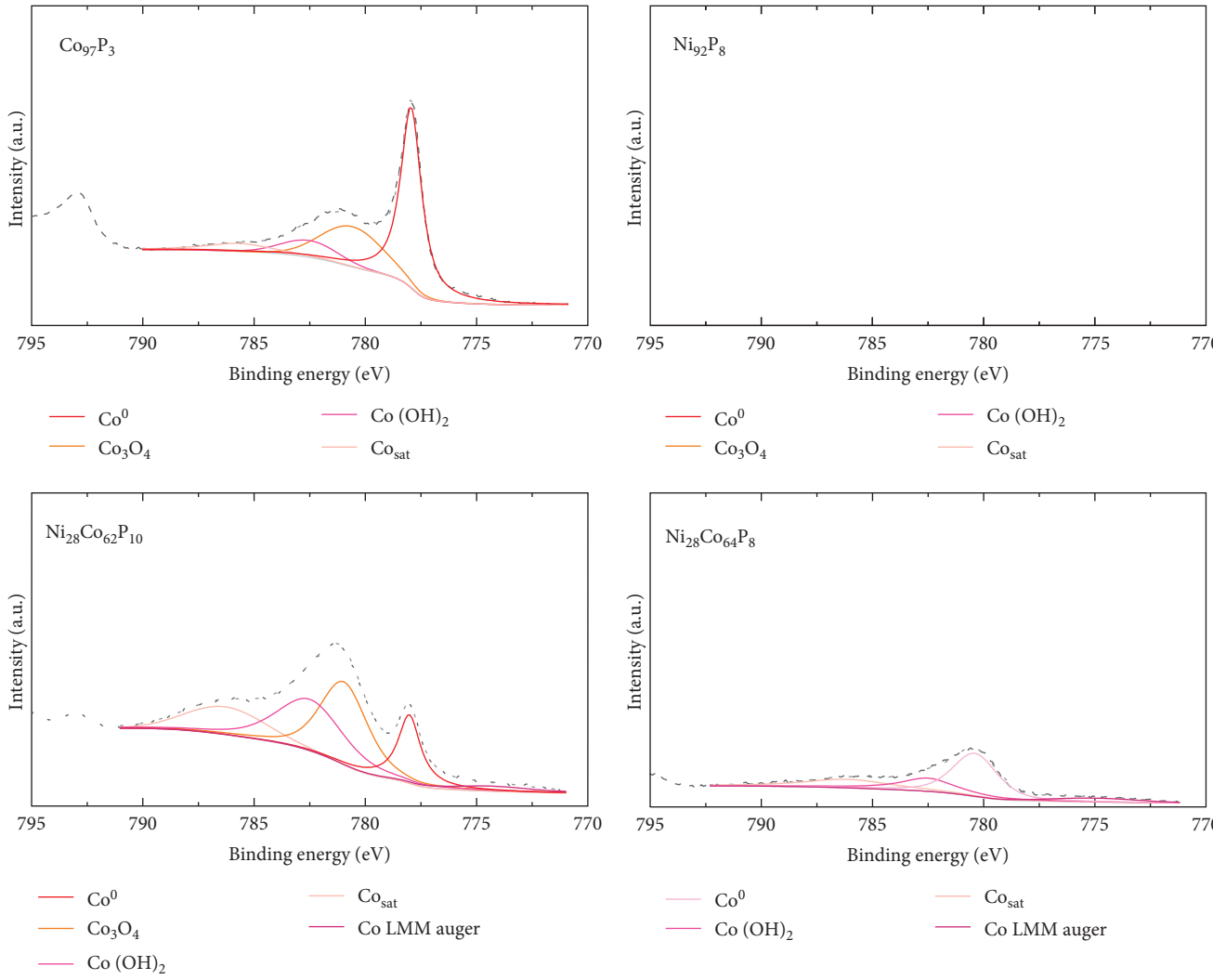

(a)

FIGURE 4: Continued.

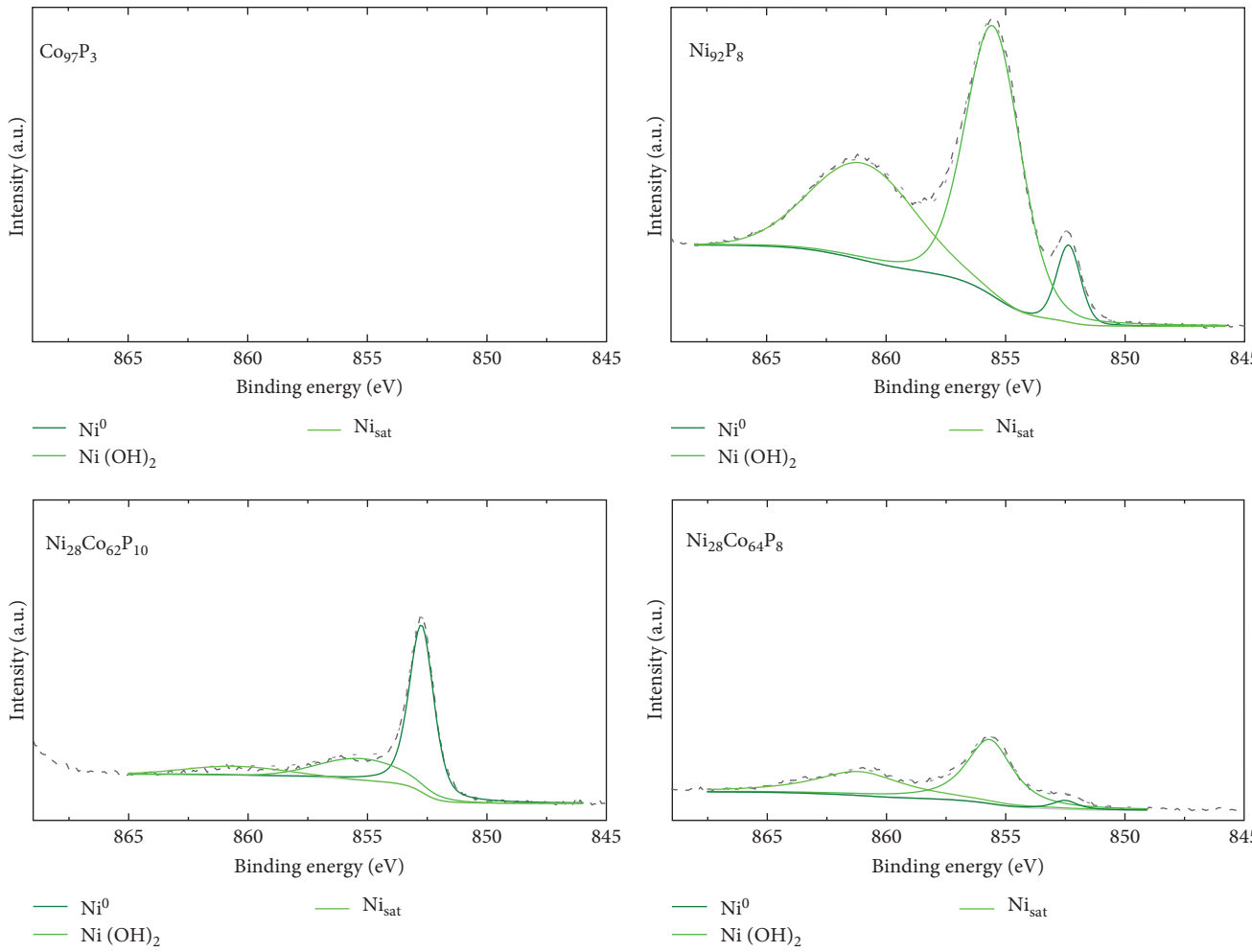

(b)

Figure 4: Continued.

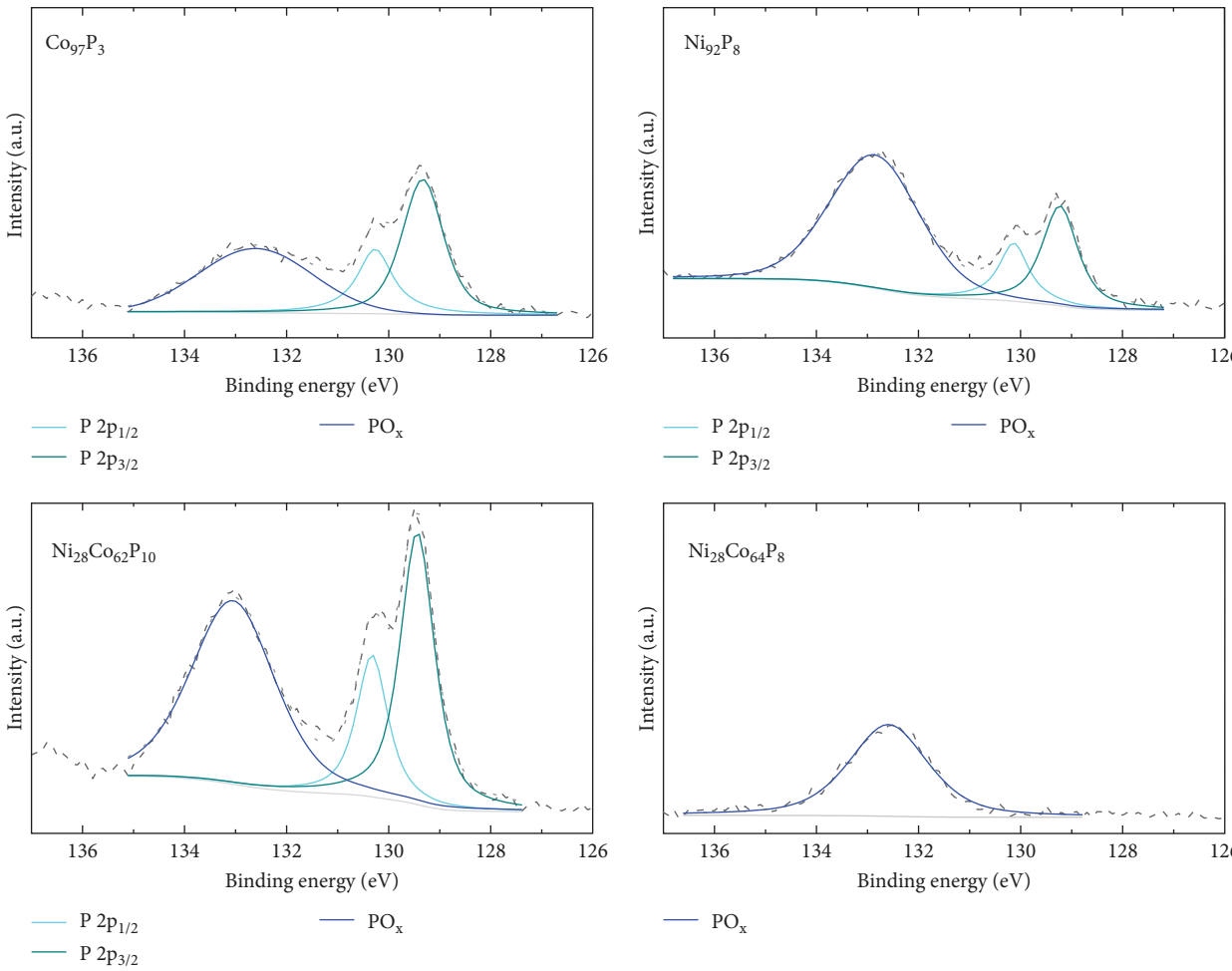

FIGURE 4: XPS spectra of (a) Ni $2p_{3/2}$, (b) Co $2p_{3/2}$, and (c) P 2p for $Co_{97}P_3$, $Ni_{92}P_8$, $Ni_{28}Co_{62}P_{10}$ and $Ni_{28}Co_{64}P_8$ (after 5000 cycles of $Ni_{28}Co_{62}P_{10}$). Raw intensity data and obtained fitting data are represented with dotted lines and dark gray short-dashed lines, respectively.

HER activity. However, excessive surface phosphates are known to form a passive layer on the catalyst surface, negatively affecting catalytic activity [69], and an optimal ratio of phosphate to phosphide likely plays a crucial role in HER performance. As evident from Figure 5c, the $Ni_{28}Co_{62}P_{10}$ catalyst, which shows the highest activity, has a phosphide/phosphate ratio close to 1. The $Ni_{19}Co_{73}P_8$ catalyst, which is the only one deviating from the trend, appears to compensate for its low phosphide/phosphate ratio with a significantly high C_{dl} (Table S1, 38.2 mF cm^{-2}) of the sample.

From the XPS analysis of CoP and NiP in Figure 4, which represent binary metal-phosphorus compounds, we can infer the preferentially formed species in each metal. This provides insights into why the formation of binary metal-phosphorus alloys is more beneficial and how these compounds influence catalyst durability. Considering that the oxidation state of metal in phosphate is higher than that in phosphide, the Co $2p_{3/2}$ spectrum of $Co_{97}P_3$ in Figure 4 reveals that metallic Co is dominant, with minor contributions from Co_3O_4 and $Co(OH)_2$. Furthermore, the P 2p spectrum indicates that the P 2p peak of Co phosphide (128–130 eV) is more pronounced than that of $Co_3(PO_4)_2$ (133–135 eV). In contrast, the Ni $2p_{3/2}$ spectrum of $Ni_{92}P_8$ consists of $Ni(OH)_2$, with only a small fraction of metallic Ni. As a result, its P 2p spectrum shows that phosphate is more dominant than phosphide for Ni. These observations suggest that in catalysts synthesized via the co-electrodeposition of Co and phosphorus, the phosphide content is greater than that of phosphate (phosphide/phosphate >1). Conversely, in catalysts formed through the co-electrodeposition of Ni and phosphorus, the phosphide content is lower than that of phosphate (phosphide/phosphate <1). This implies that both catalysts deviate from the optimal composition. Given that phosphide exhibits a more direct correlation with HER activity compared to phosphate, this phenomenon provides a rationale for the superior HER performance of CoP over NiP (Figure 3a). Compared to these monometal-phosphorus compounds, $Ni_{28}Co_{62}P_{10}$ exhibits a more balanced composition. In Figure 4, its Co $2p_{3/2}$ spectrum shows that metal oxides are more prevalent than metallic Co, whereas its Ni $2p_{3/2}$ spectrum reveals that metallic Ni is more dominant than $Ni(OH)_2$. These complementary effects result in a nearly 1:1 ratio of phosphate to phosphide, as confirmed in

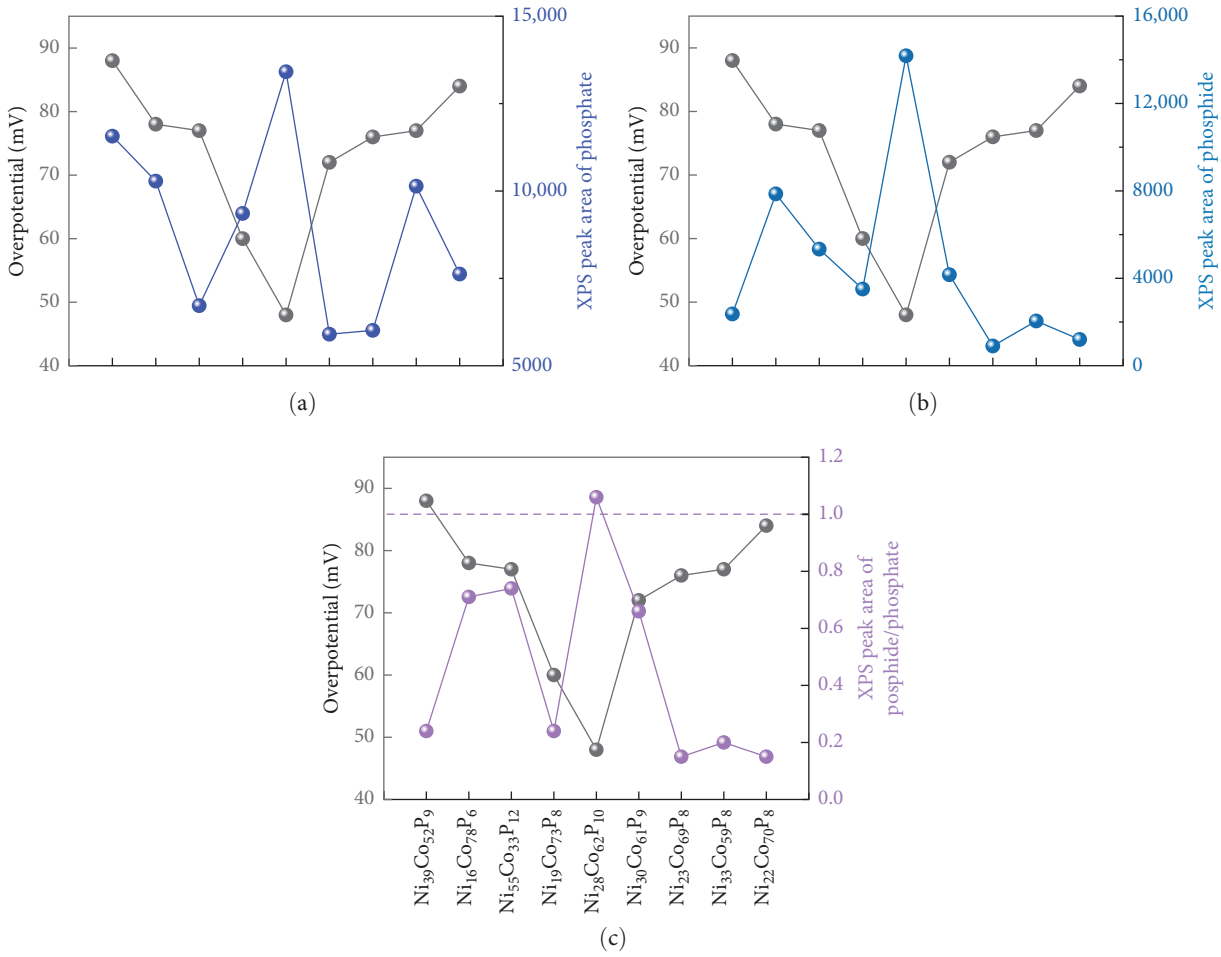

FIGURE 5: Relationship between the overpotential and the XPS peak areas of (a) phosphate, (b) phosphide, and (c) phosphide/phosphate.

the P 2p spectrum. Consequently, these findings suggest that an optimized combination of metals that preferentially form phosphate and that preferentially form phosphide can facilitate the design of more efficient transition metal-phosphorus compound catalysts.

The relationship between the ratio of phosphide to phosphate and HER activity provides a valuable framework for interpreting the performance degradation observed in the durability assessment of $Ni_{28}Co_{62}P_{10}$. After 5000 cycles of ADT, EDS analysis confirmed a compositional shift to $Ni_{28}Co_{64}P_8$. As illustrated in Figure 4, the metallic peaks of both Co and Ni decreased, accompanied by an increase in oxidation states. Additionally, the P 2p spectrum revealed the depletion of phosphide, with phosphate emerging as the dominant species. This indicates that the performance decline observed in Figure 3f over 5000 cycles is driven by the loss of phosphide, while the residual activity post-ADT is attributed to metal phosphate. These findings underscore the critical role of stabilizing metal phosphide, rather than relying solely on the inherently more stable metal phosphate, as a more effective strategy for enhancing long-term durability of metal-phosphorus compound HER catalyst.

Figure 6a presents the AEMWE single-cell performance using $Ni_{28}Co_{62}P_{10}$ as the cathode, which exhibited the highest HER activity in half-cell evaluations. The AEMWE system employing $Ni_{28}Co_{62}P_{10}$ as the cathode achieved a cell voltage of 1.88 V at a current density of 1 A cm^{-2}. Figure 6b compares the performance of the AEMWE system in this study with previously reported non-platinum-based electrodes (for both cathode and anode). The AEMWE single cell using $Ni_{28}Co_{62}P_{10}$ as the cathode demonstrates performance that is comparable to or superior to existing nonplatinum-based AEMWE systems [70–72]. Figure 6c illustrates the long-term stability of the AEMWE single cell with $Ni_{28}Co_{62}P_{10}$ as the cathode, operated at a constant current density of 1 A cm^{-2} for 100 h. The cell voltage exhibited a slight initial improvement during the first 10 h owing to activation, after which it stabilized at an average of 1.92 V. Over the 100 h operation, the degradation rate was measured at 0.21 mV h^{-1}, confirming the outstanding durability of the system.

The exceptional activity and stability of this bimetallic metal-phosphorus catalyst highlight its potential for cost-effective AEMWE commercialization. Furthermore, this study provides critical insights into the respective roles of phosphide and phosphate in alkaline HER performance, offering valuable guidance for optimizing the activity and durability of metal-phosphorus catalysts.

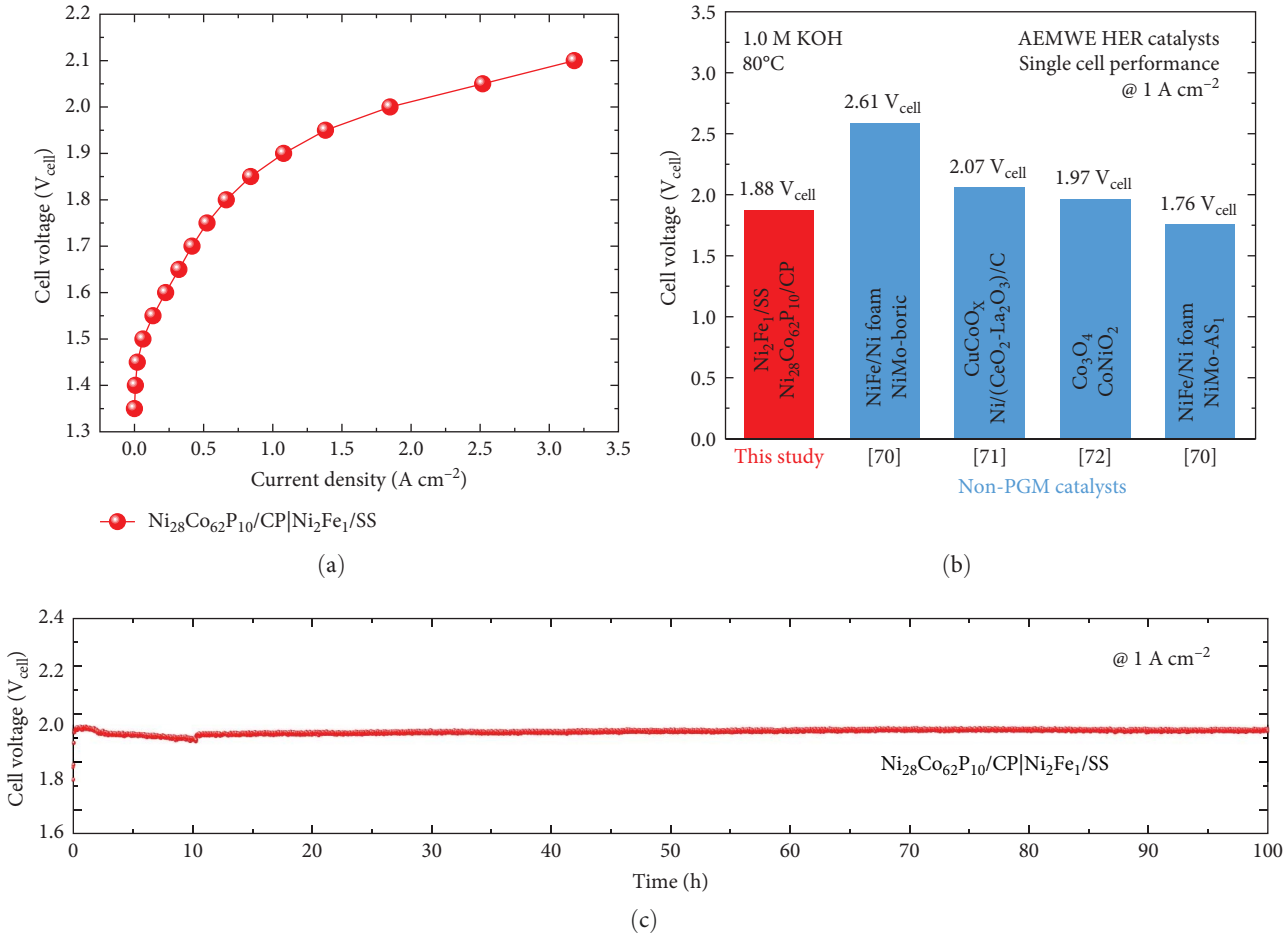

FIGURE 6: (a) *I–V* curve for AEMWE with $Ni_{28}Co_{62}P_{10}$/CP cathode and Ni_2Fe_1/SS anode, (b) cell voltage of $Ni_{28}Co_{62}P_{10}$/CP|Ni_2Fe_1/SS at 1 A cm^{-2} in comparison with literature data, and (c) 100 h durability evaluation at a current density of 1 A cm^{-2}.

4. Conclusions

This study systematically investigates the enhancement of the alkaline HER activity of transition metal-phosphorus compound catalysts, including Ni_{100}, Co_{100}, $Ni_{66}Co_{34}$, $Ni_{92}P_8$, $Co_{97}P_3$, and $Ni_{28}Co_{62}P_{10}$. Based on its surface structure, crystallinity, electrochemical properties, and HER performance, $Ni_{28}Co_{62}P_{10}$ exhibited the most outstanding HER performance because of the combination of Ni and Co and the addition of phosphorus. $Ni_{28}Co_{62}P_{10}$ exhibited a low overpotential of 48 mV at −10 mA cm^{-2} and fast charge transfer kinetics with low Tafel slope of 32 mV dec^{-1}, indicating a highly active surface and excellent electrochemical reactivity. The catalyst achieved a near 1:1 balance between phosphide and phosphate, which contributed to its high HER activity. Hence, maintaining an optimal balance between phosphide and phosphate is crucial for optimizing HER performance. Furthermore, the $Ni_{28}Co_{62}P_{10}$ catalyst maintained its high performance after more than 5000 cycles of durability testing, which demonstrated the excellent durability of NiCoP catalysts. Finally, the $Ni_{28}Co_{62}P_{10}$ catalyst showed outstanding performance in an AEMWE single-cell evaluation, achieving a cell voltage of 1.88 V at a current density of 1 A cm^{-2}, which is significantly superior to previous studies. This confirms that NiCoP-based metal-phosphorus is a promising candidate as catalyst for HER in AEMWE. These findings clarify the correlation between the compositional characteristics and electrochemical performance of NiCoP catalysts and are expected to make a significant contribution to the future development of hydrogen evolution technologies.

Data Availability Statement

The data that support the findings of this study are available from the corresponding author upon reasonable request.

Conflicts of Interest

The authors declare no conflicts of interest.

Author Contributions

Taeyoung Kim: conceptualization, formal analysis, investigation, methodology, writing – original draft. **Kyeong-Rim Yeo:** formal analysis, investigation. **Hoyoung Kim:** formal analysis, investigation. **Jinwoo Lee:** conceptualization, methodology, supervision, writing – review and editing. **Soo-Kil Kim:** conceptualization, funding acquisition, methodology, project administration, supervision, writing – review and editing.

Funding

This research was supported by the Chung-Ang University, Research Scholarship Grants in 2024 and the National Research Foundation of Korea (Grants RS-2023-00235596 and RS-2024-00413272).

Acknowledgments

This research was supported by the Chung-Ang University Research Scholarship Grants in 2024 and the National Research Foundation (NRF) of Korea grants funded by the Korean Government, MSIT (Grants RS-2023-00235596 and RS-2024-00413272).

Supporting Information

Additional supporting information can be found online in the Supporting Information section. (*Supporting Information*) Supporting data related to this article can be found online in the Supporting Information section.

References

[1] M. Y. Suberu, M. W. Mustafa, and N. Bashir, "Energy Storage Systems for Renewable Energy Power Sector Integration and Mitigation of Intermittency," *Renewable and Sustainable Energy Reviews* 35 (2014): 499–514.

[2] A. Evans, V. Strezov, and T. J. Evans, "Assessment of Utility Energy Storage Options for Increased Renewable Energy Penetration," *Renewable and Sustainable Energy Reviews* 16, no. 6 (2012): 4141–4147.

[3] M. Beaudin, H. Zareipour, A. Schellenberglabe, and W. Rosehart, "Energy Storage for Mitigating the Variability of Renewable Electricity Sources: An Updated Review," *Energy for Sustainable Development* 14, no. 4 (2010): 302–314.

[4] K. Mazloomi and C. Gomes, "Hydrogen as an Energy Carrier: Prospects and Challenges," *Renewable and Sustainable Energy Reviews* 16, no. 5 (2012): 3024–3033.

[5] A. Ursua, L. M. Gandia, and P. Sanchis, "Hydrogen Production From Water Electrolysis: Current Status and Future Trends," *Proceedings of the IEEE* 100, no. 2 (2012): 410–426.

[6] M. Wang, Z. Wang, X. Gong, and Z. Guo, "The Intensification Technologies to Water Electrolysis for Hydrogen Production—A Review," *Renewable and Sustainable Energy Reviews* 29 (2014): 573–588.

[7] T. Lim and S.-K. Kim, "Non-Precious Hydrogen Evolution Reaction Catalysts: Stepping Forward to Practical Polymer Electrolyte Membrane-Based Zero-Gap Water Electrolyzers," *Chemical Engineering Journal* 433 (2022): 133681.

[8] P. Millet, M. Pineri, and R. Durand, "New Solid Polymer Electrolyte Composites for Water Electrolysis," *Journal of Applied Electrochemistry* 19, no. 2 (1989): 162–166.

[9] U. Babic, M. Suermann, F. N. Büchi, L. Gubler, and T. J. Schmidt, "Critical Review—Identifying Critical Gaps for Polymer Electrolyte Water Electrolysis Development," *Journal of the Electrochemical Society* 164, no. 4 (2017): F387.

[10] Z. Abdin, A. Zafaranloo, A. Rafiee, W. Mérida, W. Lipiński, and K. R. Khalilpour, "Hydrogen as an Energy Vector," *Renewable and Sustainable Energy Reviews* 120 (2020): 109620.

[11] Y. Song, H. Chen, X. Wang, et al., "Engineering Ir-Based Catalysts for High Current Density Applications in Proton Exchange Membrane Water Electrolyzers," *Energy & Environmental Science* 18, no. 1 (2025): 130–154.

[12] P. Shirvanian and F. van Berkel, "Novel Components in Proton Exchange Membrane (PEM) Water Electrolyzers (PEMWE): Status, Challenges and Future Needs. A Mini Review," *Electrochemistry Communications* 114 (2020): 106704.

[13] I. V. Pushkareva, A. S. Pushkarev, S. A. Grigoriev, P. Modisha, and D. G. Bessarabov, "Comparative Study of Anion Exchange Membranes for Low-Cost Water Electrolysis," *International Journal of Hydrogen Energy* 45, no. 49 (2020): 26070–26079.

[14] M. Mandal, "Recent Advancement on Anion Exchange Membranes for Fuel Cell and Water Electrolysis," *ChemElectroChem* 8, no. 1 (2021): 36–45.

[15] H. A. Miller, "Green Hydrogen From Anion Exchange Membrane Water Electrolysis," *Current Opinion in Electrochemistry* 36 (2022): 101122.

[16] X. Li, P. F. Liu, L. Zhang, M. Y. Zu, Y. X. Yang, and H. G. Yang, "Enhancing Alkaline Hydrogen Evolution Reaction Activity Through Ni-Mn_3O_4 Nanocomposites," *Chemical Communications* 52, no. 69 (2016): 10566–10569.

[17] D. Liu, G. Xu, H. Yang, H. Wang, and B. Y. Xia, "Rational Design of Transition Metal Phosphide-Based Electrocatalysts for Hydrogen Evolution," *Advanced Functional Materials* 33, no. 7 (2023): 2208358.

[18] J. Shi, Y. Bao, R. Ye, et al., "Recent Progress and Perspective of Electrocatalysts for Hydrogen Evolution Reaction," *Catalysis Science & Technology* 15, no. 7 (2025): 2104–2131.

[19] S. Anantharaj, "Hydrogen Evolution Reaction on Pt and Ru in Alkali With Volmer-Step Promotors and Electronic Structure Modulators," *Current Opinion in Electrochemistry* 33 (2022): 100961.

[20] Z. Chen, X. Duan, W. Wei, S. Wang, and B.-J. Ni, "Recent Advances in Transition Metal-Based Electrocatalysts for Alkaline Hydrogen Evolution," *Journal of Materials Chemistry A* 7, no. 25 (2019): 14971–15005.

[21] C. Wang, W. Guo, T. Chen, et al., "Advanced Noble-Metal/Transition-Metal/Metal-Free Electrocatalysts for Hydrogen Evolution Reaction in Water-Electrolysis for Hydrogen Production," *Coordination Chemistry Reviews* 514 (2024): 215899.

[22] J. Wei, Q. Jia, B. Chen, et al., "High-Efficient Electrocatalyst of MoNi4@ MoO3-x Nanorod for Hydrogen Evolution Reaction in Alkaline Solutions," *Journal of Alloys and Compounds* 876 (2021): 160152.

[23] M. Yang, J. Zhang, W. Zhang, Z. Wu, and F. Gao, "Pt Nanoparticles/Fe-Doped α-Ni (OH)2 Nanosheets Array With Low Pt Loading as a High-Performance Electrocatalyst for Alkaline Hydrogen Evolution Reaction," *Journal of Alloys and Compounds* 823 (2020): 153790.

[24] H. G. Shiraz, X. Crispin, and M. Berggren, "Transition Metal Sulfides for Electrochemical Hydrogen Evolution," *International Journal of Hydrogen Energy* 46, no. 47 (2021): 24060–24077.

[25] Q. Gao, W. Zhang, Z. Shi, L. Yang, and Y. Tang, "Structural Design and Electronic Modulation of Transition-Metal-Carbide Electrocatalysts toward Efficient Hydrogen Evolution," *Advanced Materials* 31, no. 2 (2019): 1802880.

[26] H.-M. Zhang, J.-J. Wang, Y. Meng, and J. Sun, "Recent Advances in Amorphous Metal Phosphide Electrocatalysts for Hydrogen Evolution Reaction," *International Journal of Hydrogen Energy* 47, no. 85 (2022): 36084–36097.

[27] H. Li, X. Zhao, H. Liu, et al., "Sub-1.5 Nm Ultrathin CoP Nanosheet Aerogel: Efficient Electrocatalyst for Hydrogen Evolution Reaction at All pH Values," *Small* 14, no. 41 (2018): 1802824.

[28] W. Zhang, H. Yan, Y. Liu, et al., "Multi-Interfacial Engineering of an Interlinked Ni 2 P-MoP Heterojunction to Modulate the Electronic Structure for Efficient Overall Water Splitting," *Journal of Materials Chemistry A* 11, no. 27 (2023): 15033–15043.
[29] T. Liu, A. Li, C. Wang, W. Zhou, S. Liu, and L. Guo, "Interfacial Electron Transfer of Ni2P-NiP2 Polymorphs Inducing Enhanced Electrochemical Properties," *Advanced Materials* 30, no. 46 (2018): 1803590.
[30] R. Guo, X. Lai, J. Huang, et al., "Phosphate-Based Electrocatalysts for Water Splitting: Recent Progress," *ChemElectroChem* 5, no. 24 (2018): 3822–3834.
[31] S. Zhao, J. Berry-Gair, W. Li, et al., "The Role of Phosphate Group in Doped Cobalt Molybdate: Improved Electrocatalytic Hydrogen Evolution Performance," *Advanced Science* 7, no. 12 (2020): 1903674.
[32] Y. Li, Z. Wu, X. Zhang, et al., "Interfacial Engineering of Polycrystalline Pt5P2 Nanocrystals and Amorphous Nickel Phosphate Nanorods for Electrocatalytic Alkaline Hydrogen Evolution," *Small* 19, no. 9 (2023): 2206859.
[33] Y. Shi and B. Zhang, "Recent Advances in Transition Metal Phosphide Nanomaterials: Synthesis and Applications in Hydrogen Evolution Reaction," *Chemical Society Reviews* 45, no. 6 (2016): 1529–1541.
[34] X. Xiao, L. Tao, M. Li, et al., "Electronic Modulation of Transition Metal Phosphide via Doping as Efficient and pH-Universal Electrocatalysts for Hydrogen Evolution Reaction," *Chemical Science* 9, no. 7 (2018): 1970–1975.
[35] B. Liu, X. Lan, Q. Zhong, and T. Wang, "Metal Phosphide: An Atypical Catalytic Site," *ACS Catalysis* 14, no. 2 (2024): 757–775.
[36] A. Gubóová, R. Orinakova, M. Streckova, et al., "Bimetallic MoFe Phosphide Catalysts for the Hydrogen Evolution Reaction," *Electrochimica Acta* 506 (2024): 145008.
[37] S. K. T. Aziz, S. Sultana, A. Kumar, S. Riyajuddin, M. Pal, and A. Dutta, "Transition Metal Phosphides as Cardinal Electrocatalytic Materials for Alkaline Hydrogen Production," *Cell Reports Physical Science* 4, no. 12 (2023): 101747.
[38] L. K. Putri, B.-J. Ng, R. Y. Z. Yeo, W.-J. Ong, A. R. Mohamed, and S.-P. Chai, "Engineering Nickel Phosphides for Electrocatalytic Hydrogen Evolution: A Doping Perspective," *Chemical Engineering Journal* 461 (2023): 141845.
[39] W.-S. Kim, D. K. Cho, H. W. Lim, K.-H. Kim, S.-H. Hong, and J. Y. Kim, "Phase-Dependent Hydrogen Evolution Activity of Nickel Phosphide Nanosheet Arrays in Alkaline Electrolytes," *Electrochimica Acta* 344 (2020): 136116.
[40] S. Fu, J. Song, C. Zhu, et al., "Ultrafine and Highly Disordered Ni2Fe1 Nanofoams Enabled Highly Efficient Oxygen Evolution Reaction in Alkaline Electrolyte," *Nano Energy* 44 (2018): 319–326.
[41] Y. Park, K.-R. Yeo, Y. J. Hwang, et al., "Synergistic Enhancement of Surface-Doped Mn and Cu-Mediated Hierarchical Reconstruction in Co-Ni–Cu-Mn Electrocatalyst for Hydrogen Production in Proton Exchange Membrane Water Electrolyzer," *Journal of Alloys and Compounds* 993 (2024): 174649.
[42] A. M. Pillai, A. Rajendra, and A. K. Sharma, "Electrodeposited Nickel-Phosphorous (Ni-P) Alloy Coating: An in-Depth Study of Its Preparation, Properties, and Structural Transitions," *Journal of Coatings Technology and Research* 9, no. 6 (2012): 785–797.
[43] U. Admon, A. Bar-Or, and D. Treves, "Microstructure of Cobalt and Cobalt-Phosphorous Thin Films," *Journal of Applied Physics* 44, no. 5 (1973): 2300–2303.
[44] S. H. Hong, S. H. Ahn, I. Choi, et al., "Fabrication and Evaluation of Nickel Cobalt Alloy Electrocatalysts for Alkaline Water Splitting," *Applied Surface Science* 307 (2014): 146–152.
[45] L. Wang, Y. Gao, Q. Xue, H. Liu, and T. Xu, "Microstructure and Tribological Properties of Electrodeposited Ni-Co Alloy Deposits," *Applied Surface Science* 242, no. 3-4 (2005): 326–332.
[46] K. Mondal, N. Sathithsuksanoh, and S. B. Lalvani, "Electrodeposition and Characterization of NiCoP," *SN Applied Sciences* 2, no. 12 (2020): 1–12.
[47] Y. Shi, S. Zhou, J. Liu, et al., "An Integrated Amorphous Cobalt Phosphoselenide Electrocatalyst With High Mass Activity Boosts Alkaline Overall Water Splitting," *Applied Catalysis B: Environmental* 341 (2024): 123326.
[48] F. Zhao, H. Liu, H. Zhu, et al., "Amorphous/Amorphous Ni-P/Ni (OH) 2 Heterostructure Nanotubes for an Efficient Alkaline Hydrogen Evolution Reaction," *Journal of Materials Chemistry A* 9, no. 16 (2021): 10169–10179.
[49] J. Wang, F. Tian, L. Zhang, et al., "Double Loading of Nickel Phosphide Surface for Efficient Hydrogen Evolution Reaction," *Journal of Colloid and Interface Science* 673 (2024): 284–290.
[50] M. Wang, C.-L. Dong, Y.-C. Huang, and S. Shen, "Bifunctional Cobalt Phosphide Nanoparticles With Convertible Surface Structure for Efficient Electrocatalytic Water Splitting in Alkaline Solution," *Journal of Catalysis* 371 (2019): 262–269.
[51] N. Mahmood, Y. Yao, J.-W. Zhang, L. Pan, X. Zhang, and J.-J. Zou, "Electrocatalysts for Hydrogen Evolution in Alkaline Electrolytes: Mechanisms, Challenges, and Prospective Solutions," *Advanced Science* 5, no. 2 (2018): 1700464.
[52] F. Yang, Y. Zhao, Y. Du, et al., "A Monodisperse Rh2P-Based Electrocatalyst for Highly Efficient and pH-Universal Hydrogen Evolution Reaction," *Advanced Energy Materials* 8, no. 18 (2018): 1703489.
[53] Y. Wen, J. Qi, D. Zhao, et al., "O Doping Hierarchical NiCoP/Ni2P Hybrid With Modulated Electron Density for Efficient Alkaline Hydrogen Evolution Reaction," *Applied Catalysis B: Environmental* 293 (2021): 120196.
[54] H. Kim, H. Park, D.-K. Kim, I. Choi, and S.-K. Kim, "Pulse-Electrodeposited Nickel Phosphide for High-Performance Proton Exchange Membrane Water Electrolysis," *Journal of Alloys and Compounds* 785 (2019): 296–304.
[55] Z.-P. Lu and L. Sepunaru, "Electrodeposition of Iron Phosphide Film for Hydrogen Evolution Reaction," *Electrochimica Acta* 363 (2020): 137167.
[56] J. Huang, Y. Xiong, Z. Peng, et al., "A General Electrodeposition Strategy for Fabricating Ultrathin Nickel Cobalt Phosphate Nanosheets With Ultrahigh Capacity and Rate Performance," *ACS Nano* 14, no. 10 (2020): 14201–14211.
[57] D. Wang, Y. Wang, Z. Fu, et al., "Cobalt-Nickel Phosphate Composites for the All-Phosphate Asymmetric Supercapacitor and Oxygen Evolution Reaction," *ACS Applied Materials & Interfaces* 13, no. 29 (2021): 34507–34517.
[58] S. J. Marje, V. V. Patil, V. G. Parale, et al., "Microsheets like Nickel Cobalt Phosphate Thin Films as Cathode for Hybrid Asymmetric Solid-State Supercapacitor: Influence of Nickel and Cobalt Ratio Variation," *Chemical Engineering Journal* 429 (2022): 132184.
[59] B. Qiu, L. Cai, Y. Wang, et al., "Fabrication of Nickel-Cobalt Bimetal Phosphide Nanocages for Enhanced Oxygen Evolution Catalysis," *Advanced Functional Materials* 28, no. 17 (2018): 1706008.
[60] T. Ilyas, F. Raziq, S. Ali, et al., "Designing a Novel Cactus-Like Nickel Cobalt Phosphide Based Electrocatalyst for Hydrogen Evolution," *Applied Surface Science* 543 (2021): 148726.
[61] P. Xiao, W. Chen, and X. Wang, "A Review of Phosphide-Based Materials for Electrocatalytic Hydrogen Evolution," *Advanced Energy Materials* 5, no. 24 (2015): 1500985.

[62] L. I. Al-Ali, O. Elmutasim, K. Al Ali, N. Singh, and K. Polychronopoulou, "Transition Metal Phosphides (TMP) as a Versatile Class of Catalysts for the Hydrodeoxygenation Reaction (HDO) of Oil-Derived Compounds," *Nanomaterials* 12, no. 9 (2022): 1435.
[63] S. Budagumpi, S. Kota, M. Reddy, and D. Nagaraju, "Advanced Transition Metal Phosphide-Based Materials for Hydrogen Evolution Reactions: A Comprehensive Review," *Ionics* 31 (2025): 3965–4005.
[64] Y. Liu, X. Ma, H. Huang, et al., "Ammonia-Assisted Ni Particle Preferential Deposition in Ni-Fe Pyrophosphates on Iron Foam to Improve the Catalytic Performance for Overall Water Splitting," *Journal of Colloid and Interface Science* 665 (2024): 573–581.
[65] Y. Zhang, J. Wu, B. Guo, et al., "Recent Advances of Transition-Metal Metaphosphates for Efficient Electrocatalytic Water Splitting," *Carbon Energy* 5, no. 12 (2023): e375.
[66] D. P. Wijayanti, M. A. Nuruzzahran, D. A. Syaifullah, et al., "Hydrogen Evolution Reaction Mechanism on Pristine and Defective Nickel Phosphate Surfaces," *Results in Surfaces and Interfaces* 18 (2025): 100431.
[67] J. Xing, H. Li, M. M.-C. Cheng, S. M. Geyer, and K. Y. S. Ng, "Electro-Synthesis of 3D Porous Hierarchical Ni-Fe Phosphate Film/Ni Foam as a High-Efficiency Bifunctional Electrocatalyst for Overall Water Splitting," *Journal of Materials Chemistry A* 4, no. 36 (2016): 13866–13873.
[68] L. Yang, Z. Guo, J. Huang, et al., "Vertical Growth of 2D Amorphous FePO4 Nanosheet on Ni Foam: Outer and Inner Structural Design for Superior Water Splitting," *Advanced Materials* 29, no. 46 (2017): 1704574.
[69] X. Hu, X. Zhang, C. Pi, J. Liu, A. Lin, and K. Wu, "Study on Formation Mechanism and Corrosion Resistance of an Environmentally Protective Insulating Coating on Non-Oriented Electrical Steel," *Materials Chemistry and Physics* 304 (2023): 127819.
[70] A. Serban, M.-T. Liu, N. Chen, H. M. Chen, and X. Hu, "An Oxide-Promoted, Self-Supported Ni_4 Mo Catalyst for High Current Density Anion Exchange Membrane Water Electrolysis," *Energy & Environmental Science* 18, no. 3 (2025): 1533–1543.
[71] I. Vincent, A. Kruger, and D. Bessarabov, "Development of Efficient Membrane Electrode Assembly for Low Cost Hydrogen Production by Anion Exchange Membrane Electrolysis," *International Journal of Hydrogen Energy* 42, no. 16 (2017): 10752–10761.
[72] A. Y. Faid, A. O. Barnett, F. Seland, and S. Sunde, "Optimized Nickel-Cobalt and Nickel-Iron Oxide Catalysts for the Hydrogen Evolution Reaction in Alkaline Water Electrolysis," *Journal of the Electrochemical Society* 166, no. 8 (2019): F519–F533.